Multi-object segmentation framework using deformable models for medical imaging analysis

Rafael Namías, Juan Pablo D'Amato, Mariana del Fresno, Marcelo Vénere, Nicola Pirró & Marc-Emmanuel Bellemare

Medical & Biological Engineering & Computing

ISSN 0140-0118

Med Biol Eng Comput
DOI 10.1007/s11517-015-1387-3

Springer

Med Biol Eng Comput
DOI 10.1007/s11517-015-1387-3

ORIGINAL ARTICLE

Multi-object segmentation framework using deformable models for medical imaging analysis

Rafael Namías[1] · Juan Pablo D'Amato[2] · Mariana del Fresno[3] · Marcelo Vénere[4] · Nicola Pirró[5] · Marc-Emmanuel Bellemare[6]

Received: 4 November 2014 / Accepted: 1 September 2015

Abstract Segmenting structures of interest in medical images is an important step in different tasks such as visualization, quantitative analysis, simulation, and image-guided surgery, among several other clinical applications. Numerous segmentation methods have been developed in the past three decades for extraction of anatomical or functional structures on medical imaging. Deformable models, which include the active contour models or snakes, are among the most popular methods for image segmentation combining several desirable features such as inherent connectivity and smoothness. Even though different approaches have been proposed and significant work has been dedicated to the improvement of such algorithms, there are still challenging research directions as the simultaneous extraction of multiple objects and the integration of individual techniques. This paper presents a novel open-source framework called deformable model array (DMA) for the segmentation of multiple and complex structures of interest in different imaging modalities. While most active contour algorithms can extract one region at a time, DMA allows integrating several deformable models to deal with multiple segmentation scenarios. Moreover, it is possible to consider any existing explicit deformable model formulation and even to incorporate new active contour methods, allowing to select a suitable combination in different conditions. The framework also introduces a control module that coordinates the cooperative evolution of the snakes and is able to solve interaction issues toward the segmentation goal. Thus, DMA can implement complex object and multi-object segmentations in both 2D and 3D using the contextual information derived from the model interaction. These are important features for several medical image analysis tasks in which different but related objects need to be simultaneously extracted. Experimental results on both computed tomography and magnetic resonance imaging show that the proposed framework has a wide range of applications especially in the presence of adjacent structures of interest or under intra-structure inhomogeneities giving excellent quantitative results.

Keywords Deformable models · Segmentation framework · Multi-object segmentation · Complex segmentation · Collision control

✉ Rafael Namías
namias@cifasis-conicet.gov.ar

[1] CIFASIS, UNR-CONICET/UAM (France), Bv 27 de febrero 210 bis, Rosario, Argentina

[2] Consejo Nacional de Investigaciones Científicas y Técnicas and Instituto PLADEMA, Universidad Nacional del Centro, Tandil, Argentina

[3] Comisión de Investigaciones Científicas de la Prov. de Buenos Aires (CIC-PBA) and Instituto PLADEMA, Universidad Nacional del Centro, Tandil, Argentina

[4] Comisión Nacional de Energía Atómica (CNEA) and Instituto PLADEMA, Universidad Nacional del Centro, Tandil, Argentina

[5] Digestive Surgery Department, Hôpital La Timone, Marseille, France

[6] LSIS UMR CNRS 7296, Aix-Marseille University, Marseille, France

1 Introduction

Nowadays, the different medical image modalities aid to immeasurable improvements in the diagnosis and analysis of several patients' conditions. In the last three decades, computer-aided diagnosis (CAD) systems have become one of the major research areas in medical

Published online: 21 September 2015

imaging and diagnostic radiology [7]. Image segmentation plays an essential role in the field of image analysis for CAD systems, being a fundamental stage that determines the eventual success or failure of the later process such as visual inspection, surgical planning, treatments, or simulation. However, segmenting anatomical or functional structures from medical images is a challenging task mainly due to different image artifacts and the complexity of datasets.

Various image analysis tasks require multiple adjacent structure segmentations, for instance multiple organs in 3D abdominal CT such as liver, spleen, kidneys, pancreas, and aorta [16]); brain tumor segmentation, which comprehends white and gray matter, tumor, and edema [24]; pelvic organ prolapse, including segmentation of rectum, bladder, and uterus [2], among others. Also, other challenging tasks demand complex structure segmentations such as skull stripping in MRI [12], where the different structures of the brain are segmented; knee 3D MRI bone segmentation [6], in which different complex shaped structures may appear; and uterus delineation in dynamic MRI [14] that suffers from inhomogeneities and noise.

Several works have been proposed to resolve particular structure segmentation problems, and significant effort has been dedicated to the improvement of segmentation algorithms. Nevertheless, there are still challenging research directions on the integration of individual snake models for delimiting a single region of interest (ROI) or a group of different ROIs. Chenand Metaxas [5] have presented a hybrid segmentation framework based on deformable models, where a global energy function is introduced to combine prior-shape, region-based and boundary techniques under a fixed schema for 3D brain image segmentation. Abe and Matsuzawa [1] have proposed to use multiple active contour models (ACM) that compete with each other to segment a single object of uniform image properties as a set of subregions. More recently, Gao et al. [8] have developed a 3D multi-object segmentation tool, which not only grants mutual exclusion between regions but also parallel segmentation and models' interaction using a principle of action and reaction. The authors introduce a novel active contour formulation for that particular framework which allows to segment multiple structures but with a fixed interaction scheme for all the ROIs that limits its flexibility. Additionally, most of the proposed works focus just on multiple objects detection or complex structures segmentation, not both simultaneously.

Under level set formulations, Shang et al. [19] have developed a region competition active contour model. The algorithm is derived by minimizing a region-based probabilistic energy function and implemented in a level set framework. The model combines edge and region features in a level set evolution equation and has been extended to 3D medical structure detection. A limitation of this approach is that the competing regions are only two: the ROI and the background. Other authors (Vu et al. [22]) have used variations in the Chan-Vese formulation [4] to segment the image in more than one object plus the background searching for homogeneous intensity regions. Nevertheless, this hypothesis does not hold for some medical imaging modalities because two distinct organs can present similar intensities.

The present paper proposes an open-source segmentation framework named deformable model array (DMA), to be used for medical segmentation tasks involving multiple and complex object detections. For this purpose, DMA enables using a combination of existing or new explicit deformable models (DM) in an efficient and transparent way. Thus, DMA allows considering several segmentation strategies, for instance simple segmentation (one ROI only), multiple object segmentation (simultaneous detection of several ROIs, adjacent or isolated), and complex object segmentation (ROI with complex shape or different image characteristics), including a novel model cooperative interaction scheme. The framework can deal with image data in both 2D and 3D scenarios, and one of its main advantages is the possibility to easily include a set of DM algorithms to quickly develop and test segmentation strategies in almost any existing medical imaging modality.

2 Methods

In order to be extensible and adaptable to diverse segmentation problems, the framework must deal with different images modalities (e.g., MRI, CT) and dimensions: 2D and 3D. Although there is not a segmentation technique which can achieve high-quality results in any scenario, the correct election of existing state-of-the-art techniques or the development of a particular new method could solve this issue. Explicit deformable models have several advantages, specially for parallel and interacting segmentation since their capability to incorporate control mechanism such as evolution restrictions, collision detection, and shape guidance.

Moreover, DMA can deal with several segmentation strategies thanks to its ability to use several DM in a cooperative way. Therefore, one of the main contributions of DMA is its evolution control (EvCtrl) module, which was specially designed for this purpose. The framework is open source, implemented mainly as filters over the ITK libraries [25] and its graphical user interface in Qt. ITK has become

one of the most complete open-source medical image processing libraries adding new state-of-the-art techniques in each new release version. The sources are publicly available.[1] In the following, we describe the general DMA formulation and its main components.

2.1 Global scheme

The required input data comprise the image to segment, a set of initial models, called evolving models (e_M), and a set of deformable model techniques (dm_T) to evolve the e_M, as well as the parameters of each dm_T. Hence, these two items are grouped in tuples (e_M, dm_T), one for each ROI. Next, DMA enables to use previous segmentation knowledge representing a set of spatial restrictions named as fixed models (f_M). Finally, a few framework parameters, later described, must be set to run the segmentation. Consequently, a convenient GUI was designed using the Qt libraries [3] to facilitate the DMA experiment setup, enabling to save and load the complete project state, visualize the scene, etc.

The framework is composed by a set of functional modules. The EvCtrl module is the main component which comprises the novel cooperative functionality and governs the evolution process. Its three main interrelated tasks are the evolution process, the collision detection, and the state management. A collision detector (ColD) module is used to evaluate whether any *inter-* or *intra-*collision occurs during the models evolution. We consider a collision as the intersection of two or more non-neighboring elements in the geometrical model representation. As this task has high computational overhead, particularly in 3D, an efficient ad hoc classification technique was implemented. In addition, a safe-state (SS) module is considered one for each e_M, which keeps a history of previous model states and the last known state without collisions. This module is crucial, as it determines whether to continue the evolution of the models. A ColR module is concerned with solving the presence of collisions, interacting with each dm_T to solve these intersections. Finally, we obtain the segmentation result represented by the final state of each input e_M.

The global segmentation process is shown in Fig. 1. The image of interest together with the models' initialization is provided to the algorithm: in green the e_M, and in red the f_M. The EvCtrl module governs the evolutions and interactions of the models until they finish the segmentation process. Finally, if a complex structure segmentation takes place, the post-processing assembles the models comprising the final complex structure.

[1] http://www.cifasis-conicet.gov.ar/namias/Files/Filters/DMA_Framework_Qt5.tar.gz.

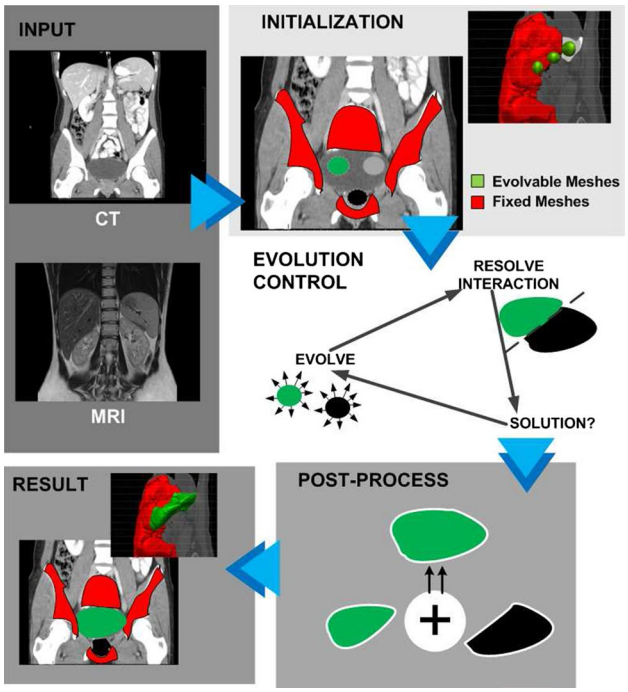

Fig. 1 DMA global segmentation process

2.2 Modules

2.2.1 Evolution control

The EvCtrl module is the main coordinator of the segmentation process. Its main task is to synchronize all the dm_T and control their interactions. Its inputs are the above-presented elements: $e_M + f_M$ models, the dm_T with all their parameters, the input image and a *synchronization distance* parameter $N \in \mathbb{N}^+$. Each e_M has one instance of an SS module, and one instance of the dm_T. The SS keeps a history of previous states of its particular e_M and will be able to restore its state to the last collision-safe state or *checkpoint* whenever is required by the EvCtrl. The dm_T guides the e_M evolution across the iterations. The last EvCtrl part is the ColD module. This module tracks the e_M evolutions and interactions, looking for collisions between or inside each e_M.

The EvCtrl module first calls the ColD to check for initial collisions and the SS module to save the first safe states. Then, the evolution loop starts: every dm_T do N iterations; consequently, the *ColD* checks for collisions, and if any occurs, the EvCtrl asks the diverse dm_T to solve the collision problems. Finally, the new *checkpoint* is saved in the SS module. The loop continues until all dm_T finish their evolution.

We define *context information* as the knowledge provided by the model interaction, generally as a spatial

restriction coming from both the f_M and the e_M during the segmentation process under the framework formulation.

2.2.2 Safe states

The SS module keeps a list of e_M states along with the iteration number when it is saved and the last collision-free state or *checkpoint*. The SS uses these saved states to restore the models to a safe configuration before mesh overlapping. During evolution, whenever it is necessary, the EvCtrl can rollback the e_M to any of the saved states, apply a collision solution to the problematic nodes, and re-evolve the e_M toward the current synchronization point.

2.2.3 Collision detector

This module implements a ColD algorithm. The algorithm concerns with the detection of intersecting elements from different models or elements of the same model (self-collisions). It is worth noting that if a collision is not solved, the segmented models are invalid, as the meshes are struggling or overlapping. Hence, a ColD should search potential elements in conflict efficiently, and if a collision is detected, some resolution strategy should be taken. Elements' collision checking is performed several times, almost for every iteration, adding a high computational cost to the process.

As the ColD is mainly dependent on the snake model representation, it is important to consider the space dimension to instantiate the particular ColD. Therefore, in 2D, it is necessary to implement a segment intersection routine, but if we are dealing with a 3D space, the algorithm must handle spatial triangle intersections.

2.2.4 Improved collision detection strategies

In real-time solutions, grids or kd trees are good approaches to find elements in space. Some works consider that initial meshes are distant from each other, and many evolution steps are required before a collision appears. Nevertheless, this assumption is not completely true, and collisions should be checked every a small number of step, with a high computational cost, even with classification schemes. Generally, the detection time is higher than the snake evolution time.

A simple strategy to reduce the computational cost even more is to do one collision check after a fixed number of evolution steps N. If a collision is detected at the end of the interval, the EvCtrl goes back to a safe state, resolves the collision, and continues. However, if N is large, intersections could be detected distant from the actual collision iteration. When this occurs, models tend to distort. On the contrary, if N is small, the computational cost is high; nonetheless, the borders' proximity is tighter. This checking strategy has a collision checking cost of $\Theta(\frac{K}{N})$ where K is the total number of evolution steps.

To improve the collision detection algorithm, we implement another strategy called *substep checking*. We still check for collisions each N step but saving all the intermediate states (element positions and forces). If no collisions are detected after N steps, these states are erased. Otherwise, we use a binary search through the saved states to efficiently find the first collided state iteration. Thus, the total detections required for the *substep checking* strategy are $\Theta((K \log N)/N)$.

2.2.5 Collision resolution strategies

The final module implements a collision resolution strategy in collaboration with the dm_T involved to avoid further intersections.

A simple but effective method to solve collisions is to *freeze* colliding elements. These elements are marked, and they are no longer updated in the next evolution steps. Another option, instead of freezing elements, is to use a proportional repulsive force opposite to the movement of each colliding element [21]. Even though it is a more general approach, it is unstable and, in the studied cases, leads to a similar result as the freezing strategy, and at a higher cost.

3 Results

3.1 Experiments

We introduce five challenging real-case medical segmentation examples where the framework capabilities are highlighted. The first example is a 2D segmentation problem involving multiple and complex pelvic organs in MRI. The uterus borders have low contrast, and its inner region has high signal inhomogeneities making it very difficult to segment using a single DM. Namias et al. [14] remark the segmentation for this problem. Second, two segmentation tasks of adjacent volumetric objects are included: heart segmentation in CT and brain tumor segmentation in MRI. On the one hand, the soft tissue in CT imaging has low contrast making it complicate to segment by common dm_T. On the other hand, DMA enables to segment multiple tumors simultaneously. Finally, two segmentation examples of complex structures in CT are shown where the presence of obstructing matter completely changes the image intensity inside the ROI.

We have considered two traditional dm_T for the experiments: T snakes [13] and GVF snakes [23], which are briefly described in the "Appendix," since their capabilities and previous experience of the authors. The experimental

Table 1 Experiment configuration and parameters

Case	Input meshes	Image	DMA parameters
Pelvic organ segmentation	Uterus: $e_M = 3$Bladder: $e_M = 1$, $f_M = 2$ (fat, rectum)	T2 256 × 256 MRI DICOM	T snakes, 2D ColD ($N = 25$)
Heart segmentation	Heart: $e_M = 1$. $f_M = 6$ (lungs, liver, cava, aorta, stomach)	512 × 512 × 167 CT DICOM	T snakes, 3D ColD ($N = 25$)
Tumor segmentation	Tumor: $e_M = 1$, $f_M = 2$ (white and gray matter)	128 × 128 × 90 MRI DICOM	GVF snakes, 3D ColD ($N = 15$)
Colon segmentation	Missing sections: $e_M = 2 \sim 3$, $f_M = 2$ (colon sections)	512 × 512 × 562 CT DICOM	T snakes, 3D ColD ($N = 25$)
Stomach segmentation	Stomach: $e_M = 3$	512 × 512 × 218 CT DICOM	GVF snakes, 3D ColD ($N = 15$)

parameters are summarized in Table 1. The experiments were ran in an Intel(R) Core(TM) i5-3570 CPU @ 3.40 GHz with 16 Gb RAM and Linux kernel version: 3.11.0-23-generic.

The segmentation results are validated against the ground truth (GT) given by the physician or available online. For the 2D experiments, we use the Dice similarity coefficient:

$$\mathcal{D}(A,B) = \frac{2 \times |A \cap B|}{|A| + |B|} \tag{1}$$

where A is the reference pixel set, and B is the DMA resulting pixel set. To compare the 3D surfaces, we directly evaluate the volumetric differences using a ray cast technique over the triangular meshes models according to the following volumetric coefficient metric:

$$\mathcal{M}(A,B) = 1 - (f_n + f_p) \tag{2}$$

$$f_n = \frac{V_{A/B}}{V_A \bigcup V_B} \quad \text{and} \quad f_p = \frac{V_{B/A}}{V_A \bigcup V_B} \tag{3}$$

where f_n is the false-negative rate, f_p is the false-positive rate, V_A is the volume of the reference model A, and $V_{A/B}$ is the volume difference between A and B. In a similar way, V_B is the volume of the DMA resulting model B, and $V_{B/A}$ is the volume difference between B and A. Both quality metrics lie between 0 and 1 where 0 means no similarity and 1 a total similarity. With the only purpose of presenting the framework capabilities in the following experiments, we used a manual initialization. Even though automatic model initialization could be done for each specific case, this issue is out of the scope of this paper.

3.2 Multiple organ segmentation in dMRI (2D)

In this section, we present the segmentation of two adjacent pelvic organs: bladder and uterus vagina set (UV-S), under *T2-weighted* dynamic magnetic resonance imaging (dMRI) for prolapse diagnose. The dataset was acquired with informed consent of the patients, taken in the sagittal midline by specialists at the Hôpital La Timone, Marseille, France [17], also used in [14, 18]. The segmentation stage comprises a fundamental part in the MoDyPe project[2] supported by the French National Research Agency under reference ANR-09-SYSC-008. In *T2-weighted* images, the uterus segmentation represents a challenging goal due to its heterogeneous boundary and narrow shape [14].

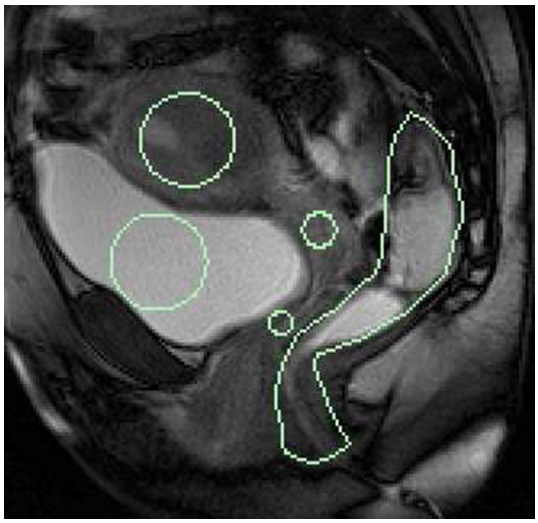

Fig. 2 Uterus and bladder segmentation in sagittal midline MRI. e_M (*circles on the left*) and f_M (*right*)

An initialization example is shown in Fig. 2. We use previous segmentations of the rectum as *context information* (Fig. 2, on the right). We use only one e_M for the bladder and three for the UV-S representing the uterus body, the cervix and the vagina. All dm_T are T snakes.The UV-S set delimitation is particularly difficult because of its intensity inhomogeneities. For this reason, we employ a three e_M set to segment this complex structure. The UV-S region is represented by the union of the e_M final states.

[2] http://modype.lsis.org.

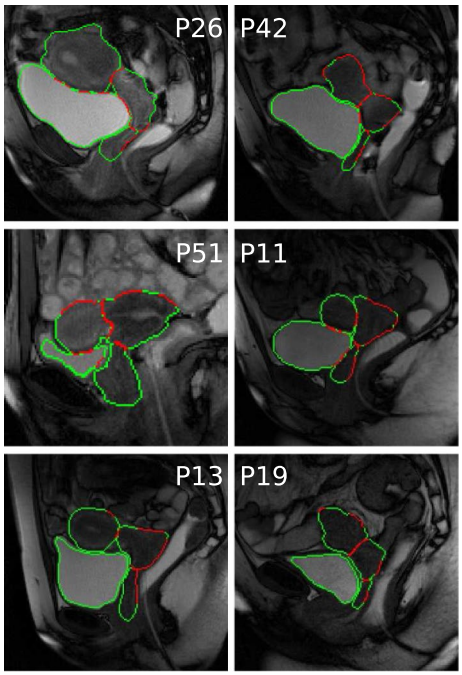

Fig. 3 Bladder and UV-S final DMA results in six patients. In *red,* the collided segments; in *green*, the non collided (color figure online)

Table 2 Multiple organ segmentations, quantitative comparison using Dice similarity against GT

	Bladder	UV-S
P11	0.967	0.864
P13	0.936	0.871
P19	0.957	0.862
P26	0.942	0.855
P42	0.921	0.882
P51	0.865	0.920

3.2.1 Results

We include six patients. This multi-object segmentation experiment exploits most of the capabilities of the framework. Firstly, we segment the bladder and the UV-S simultaneously, using the prior rectum segmentations as constraints. Some qualitative results are shown in Fig. 3. In green, the segments that did not collide are depicted, and in red the collided elements. On the one hand, the bladder contours are mostly green as they rarely interact with the UV-S contours. On the other hand, the UV-S borders interact with each other and with the rectum constraint (on the right). Although the f_M are omitted in the figure, they were considered as constraints. Dice coefficients of the segmentation results against the GT given by the physician are summarized in Table 2. As can be seen, DMA achieves excellent results, particularly in the UV-S, despite the images intrinsic difficulties.

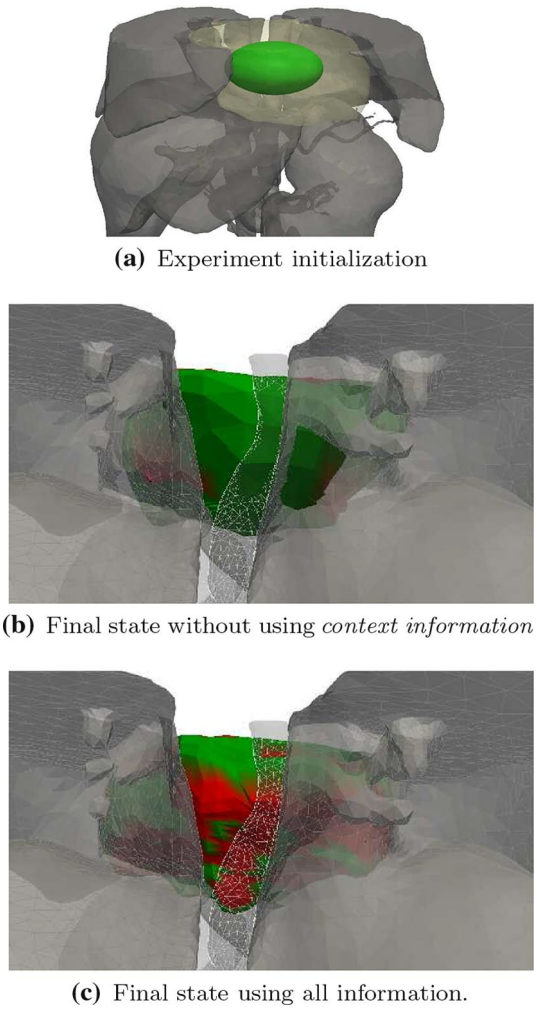

(a) Experiment initialization

(b) Final state without using *context information*

(c) Final state using all information.

Fig. 4 Experiment mesh representation. **a** The initial e_M (*in green*), ground truth (*in translucent yellow*), and surrounding organs f_M (*in gray*). **b**, **c** In *green* the evolving elements, and in *red* the frozen ones for the different runs (color figure online)

3.3 Context information evaluation

The next two experiments highlight the importance of the *context information* derived from DMA formulation.

3.3.1 Heart segmentation in CT

In this experiment, we use a public dataset from the *3D Image Reconstruction for Comparison of Algorithm Database*[3] [20] called 3D-IRCADb-02, which is composed of two anonymized abdominal enhanced 3D CT scans. The first

[3] http://www.ircad.fr/fr/recherche/3d-ircadb-02-fr/.

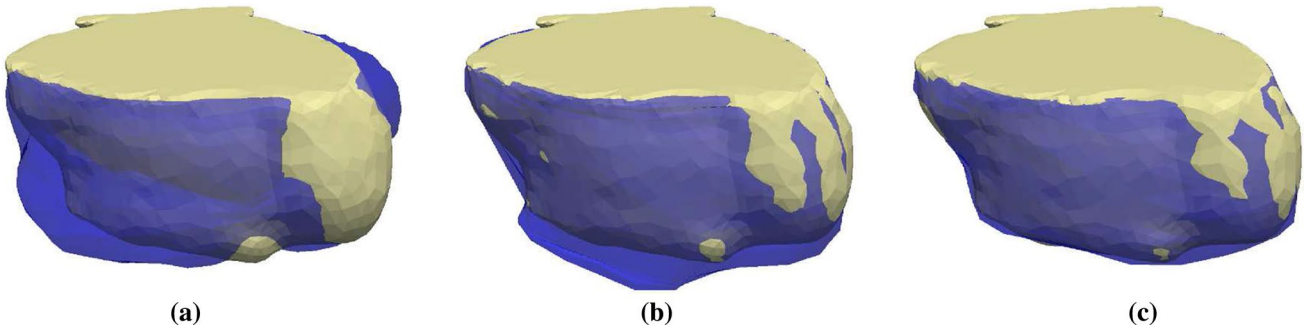

Fig. 5 Segmentation comparison between DMA result (*blue*) and the GT (*yellow*) using: **a** *context information*, **b** image information and **c** DMA image and *context information* (color figure online)

Table 3 Quantitative comparison of the different information usage during segmentation

Information	$\mathcal{M}$	f_p	f_n
Context	0.765	0.183	0.052
Image	0.845	0.089	0.066
Both	0.892	0.075	0.033

acquisition has been made during the arterial phase in inhaled position. The dataset provides the ground truth segmentation of the principal organs as DICOM images and also triangular surface meshes. We segment the heart using the ground truth meshes of the surrounding organs (lungs, stomach, liver, and vena cava) as constraints. The constraint organ meshes are shown in gray in Fig. 4a, the model initialization in green, and the GT in yellow. We present three different runs. The first run sets the parameter configuration leading to a model expansion using no image information (nullifing the gradient external force). The second run employs all the standard forces but not the *context information*. Finally, the third run utilizes all of the available information.

3.3.2 Results

The first run shows the importance of the *context information* since just using this piece of information, the dm_T can achieve an acceptable segmentation quality ($\mathcal{M} = 0.765$). As the e_M does not use image information to guide their evolution, the results should over-segment the heart since the e_M only stops when it collides with an f_M. This phenomenon is remarked in the f_p column of the context experiment in Table 3. The f_p representing the over-segmentation phenomenon depicts the greatest error overall.

In the second run, a standard segmentation is performed. Despite having a better overall segmentation metric ($\mathcal{M} = 0.845$) and half of the f_p volume compared to the first run, Fig. 4b shows that the e_M intersects boundary organs, especially the liver and the stomach.

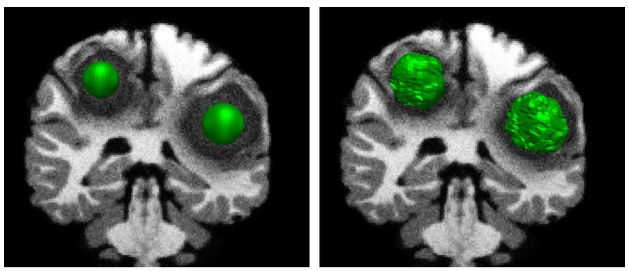

Fig. 6 MRI tumor segmentation. **a** Experiment setup. One e_M for each tumor (*green*). **b** DMA result (color figure online)

The final experiment used all of the available information. In this case, the e_M molded to the surrounding organs (Fig. 4c) and obtained the best result ($\mathcal{M} = 0.892$) with the lowest f_p and f_n volumes.

The analytic results are visually confirmed in Fig. 5. Figure 5a shows over-segmentation of the DMA result using *context information* (in blue) against the ground truth (in yellow). In Fig. 5b, even though the false-positive rate is reduced due to the image information, there are some over-segmented pieces. Finally, Fig. 5c shows the best result using both image and *context information*.

3.3.3 Tumor segmentation in MRI

This experiment consists in tumor segmentation in MRI. Brain tumor image data used in this work were obtained from the *MICCAI 2012 Challenge on Multi-modal Brain Tumor Segmentation*[4] [11]. We employ four simulated brain MRI from the dataset including the simulated image *SimBRATS_HG0004* which has two tumors (Fig. 6). First, we segment the white and gray matter, and the meshes are used as *context information* in the experiments. To segment the

[4] http://www.imm.dtu.dk/projects/BRATS2012.

Table 4 Tumor segmentation experiment

Dataset	No context			With context		
	$\mathcal{M}$	f_p	f_n	$\mathcal{M}$	f_p	f_n
1	0.867	0.019	0.114	0.936	0.003	0.061
2	0.848	0.022	0.130	0.890	0.002	0.108
4_1	0.593	0.365	0.042	0.879	0.003	0.118
4_2	0.682	0.265	0.053	0.843	0.005	0.152
7	0.832	0.121	0.049	0.895	0.003	0.102

Context information versus stand-alone snake technique

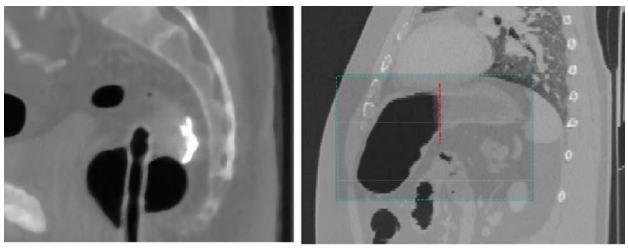

(a) (b)

Fig. 7 Occlusion examples in CT. **a** Rectum occluded region in a CTC. **b** Stomach occluded region from the IRCAD dataset. Heterogeneous region limit in *red line* (color figure online)

tumors, the deformable models were initialized with a spheric model (Fig. 6a), and a GVF snake formulation was applied (Fig. 6b).

3.3.4 Results

For the two tumors image, one e_M was used for each one. We highlight this special case because we could segment both tumors simultaneously using DMA. In this experiment, the usage of *context information* improved the stand-alone snake segmentation process as shown in Table 4. As expected, the f_p is considerably reduced using *context information* what avoids over-segmentation. *Context information* is particularly important in cases where the tumors location context and the extended edema present similar intensities. Under these conditions, the stand-alone snake had lower-quality results than DMA (4_1 and 4_2, Table 4).

3.4 Obstructions in CT

In CT imaging, some anatomic structures can feature remarkable heterogeneous image intensities. A representative example is the digestive system where there is a mixture of air, liquids, food, and fecal material. Under these circumstances, a simple segmentation strategy fails to properly segment the organ of interest. Nevertheless, the DMA framework can handle this issue. We present two occlusion segmentation examples: colon segmentation and stomach segmentation. A sagittal view of the rectum in a CT colonography (CTC) is shown in Fig. 7a. Feces, rather than dark(air), appear in the rectum with a brighter signal intensity hampering the segmentation task. A sagittal view of the stomach is depicted in Fig. 7b. Likewise, the presence of food, liquids, and air produces two distinctive signal intensities.

3.4.1 Colon segmentation

In this case, we use an anonymized public colonoscopy computed tomography (CTC) image from the National Cancer Institute Image Cancer Archive.[5]

Some images present obstructions because of liquid and fecal matter. These obstacles lead the automatic segmentation algorithm to fail. Two experiments are depicted in Fig. 8: in red, the previous segmentation result of the algorithm described in [15] and DMA e_M initialization in green, respectively. The problematic regions have a noisy decaying intensity signal and narrow shapes. Therefore, we initialized the ROI with multiple T snake models. The final meshes' configuration is shown in the right column.

Results DMA was applied in five CTCs of the dataset where different sections were obstructed. No quantitative measures are presented because the missing found portions are about 4−8 % of the total volume of the ROI, giving a minimum variation in the $\mathcal{M}$ index (∼0.05 %). In all cases, DMA managed to complete and connect the pending sections (Fig. 8a, b on the right).

3.4.2 Stomach segmentation

The second occlusion experiment also uses the acquisitions from the 3D-IRCADb-02 dataset. We segmented the stomach in two images. In both cases, we set three e_M, two for the dark region and one for the bright one as shown in Fig. 9a. No *context information* was used.

[5] http://cancerimagingarchive.net/.

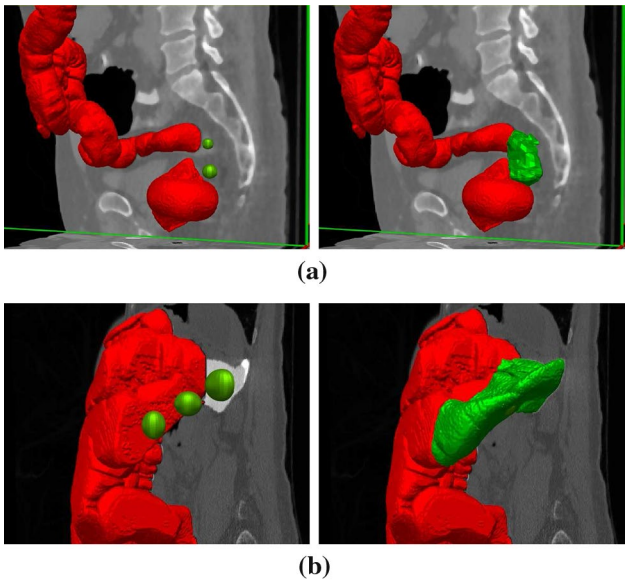

Fig. 8 CTC colon obstruction problems. Experiment setups on the left. Previous segmentation results (*in red*) acting as f_M. The e_M in *green*. Mesh representation of the segmentation result over the CT on the right **a** rectum, **b** descending colon (color figure online)

Table 5 Stomach segmentation performance

Case	$\mathcal{M}$	f_p	f_n
IRCAD2.1	0.890	0.006	0.104
IRCAD2.2	0.865	0.003	0.132

3.4.3 Results

Table 5 summarizes the segmentation results. DMA achieves good results in both cases, even though there are high f_n rates because the method under-segments the ROI. A sagittal view of the segmentation result is presented in Fig. 9c. The dotted lined circles show where the under-segmentation occurs, being the most difficult areas to include because of intensity variations, concave shape, and models interaction that make models stop distant from the real borders.

4 Discussion

The real-case experiments included several segmentation strategies available on DMA, for instance, simple segmentation with constraints (heart), multiple segmentation (tumors), and complex segmentation (stomach and colon), and both complex and multiple segmentations (pelvic organs) which included CT and MRI imagery in 2D and 3D, and multiple dm_T, showing the adaptability and wide branch of potential applications for the framework.

More precisely, in the uterus and bladder example, we segmented both a complex structure and a simple one simultaneously. The e_M evolved in parallel and competed against each other to advance toward the organs borders. In the heart and tumor experiments, we simulated a sequential segmentation where we used previous knowledge such as f_M to evaluate the importance of the contextual information. The DMA results show that the *context information* improved the stand-alone snake results reducing the false-positive rate, but sometimes increasing the false-negative error. Then, we presented a concrete segmentation application where the DMA formulation is specially advantageous. We introduced two examples including colon and stomach segmentation in CT with obstruction problems. We took advantage of the framework characteristics to straightforwardly solve complex structure segmentation scenarios where previous works needed two or more different segmentation steps. A fair comparison between DMA and existing methods is hard because the latter cannot not model these complex scenarios as a whole.

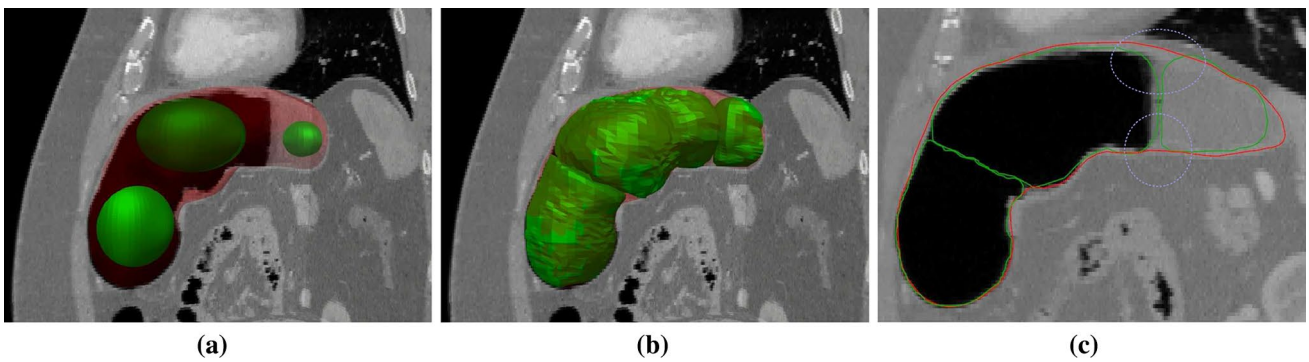

Fig. 9 Stomach segmentation experiment over complex structure ROI. **a** Experiment setup over the CT. In *translucent red* the GT, in *green* the e_M initialization. **b** DMA segmentation result. **c** Under-segmentation problems (color figure online)

In all cases, collision detection plays an outstanding role. Mesh collisions are detected and managed, both in 2D and 3D using different image modalities. It provides the usage of previous knowledge, in the form of meshes, as spatial restrictions to the e_M. The explicit use of *context information* is a contribution since no previous works stand out its importance and benefits.

5 Conclusion

A novel open-source framework for multi-object segmentation in medical images was presented. The framework allows using and combining any explicit deformable model technique to perform segmentation tasks under different modalities in a transparent way. One of the main contributions of this proposal is the incorporation of a control scheme to coordinate the evolution of the models and resolve interaction issues. This module not only helps to prevent object overlapping or leakage, but also provides a mechanism to introduce context information from the other ROIs as fixed models. This piece of information has an important relevance since it improved; in some occasions, the stand-alone technique segmentations result. Other relevant contribution is its possibility to work under several segmentation conditions: sequentially, by first segmenting the "simple" objects, converting them to fixed models and then "hard" ones, or, in parallel, evolving multiple models that compete to segment different ROIs. The experimental results showed great adaptability to a wide range of medical imaging scenarios.

Although only two classic dm_T were employed, DMA can easily integrate any explicit method. Moreover, for the collision resolution module, other strategies could be incorporated, which should be considered as future work. Nevertheless, we think that using, for instance, a repulsion force would lead to similar results increasing the computational cost.

Appendix: Snake formulations

Snakes are explicit deformable models that can evolve toward an object boundary within the image under the influence of internal forces and external forces. After the initial proposal of Kass et al. [10], several formulations have been proposed [9]. In this paper, we consider two well-known DM techniques as examples. The first method is based on the T snake formulations proposed by McInerney and Terzopoulos [13], and the second is the gradient vector flow snakes (GVF snakes) presented by Xu and Prince [23].

T snake formulation

T snake-based methods are discrete approximations to a conventional parametric snakes model while retaining many of its properties. The model is geometrically represented by a closed polygonal for 2D problems and by a triangular surface mesh for 3D. The deformation of the snake model is governed by discrete Lagrangian equations of motion, and each element $\mathbf{x}(t)$ evolves according to the following motion equation:

$$\mathbf{x}(t+1) = \mathbf{x}(t) - \Delta t(a\alpha(t) + b\beta(t) - p\rho(t) - q\mathbf{f}(t)) \quad (4)$$

where α, β are the internal forces (tension and flexion), $\mathbf{f}$, ρ are the external forces (balloon and image gradient forces), and a, b, p and q are the force weighting parameters.

The T snake formulations modify the original external force adding an adaptive inflation force $\rho(t)$ term depending on the image intensity features.

$$\rho(t) = F(I(x(t))) \cdot \mathbf{n}(x(t)) \quad (5)$$

where $\mathbf{n}$ is the unitary normal vector to the model, and F is a binary function relating ρ to the intensity field of the image I:

$$F(I(x(s,t))) = \begin{cases} +1 & \text{if } \frac{|I(x(s,t)) - CI(r)|}{k\sigma(r)} \leq 1 \\ -1, & \text{otherwise} \end{cases} \quad (6)$$

where $CI(r)$ is the characteristic intensity of the ROI, $\sigma(r)$ is the ROI intensity deviation, and k is an input parameter.

GVF snake formulations

Gradient vector flow (GVF) snakes introduce a new external force for active contour models. The difference between traditional snakes and GVF snakes consists in that the latter converge to boundary concavities and they do not need to be initialized close to the boundary [23].

To improve the original snake formulation, the authors introduced a non-irrotational external force field $v(x,y) = [u(x,y), v(x,y)]$ known as GVF field. The field is calculated as a diffusion of the gradient vectors of a gray-level or binary edge map:

$$GVF = \iint \mu(u_x^2 + u_y^2 + v_x^2 + v_y^2) + |\nabla f|^2 |v - \nabla f|^2 \mathrm{d}x\mathrm{d}y \quad (7)$$

where μ is an input parameter.

References

1. Abe T, Matsuzawa Y (2000) A region extraction method using multiple active contour models. In: Proceedings of the IEEE conference on computer vision and pattern recognition, 2000. IEEE, vol 1, pp 64–69

2. Bay T, Chambelland JC, Raffin R, Daniel M, Bellemare ME (2011) Geometric modeling of pelvic organs. In: 2011 annual international conference of the IEEE engineering in medicine and biology society, EMBC. EEE, pp 4329–4332
3. Blanchette J, Summerfield M (2006) C++ GUI programming with Qt 4. Prentice Hall Professional
4. Chan T, Vese L (2001) Active contours without edges. IEEE Trans Image Process 10(2):266–277
5. Chen T, Metaxas D (2005) A hybrid framework for 3d medical image segmentation. Med Image Anal 9(6):547–565
6. Dodin P, Martel-Pelletier J, Pelletier JP, Abram F (2011) A fully automated human knee 3d MRI bone segmentation using the ray casting technique. Med Biol Eng Comput 49(12):1413–1424
7. Doi K (2005) Current status and future potential of computer-aided diagnosis in medical imaging. Br J Radiol 78(suppl1):s3–s19
8. Gao Y, Kikinis R, Bouix S, Shenton M, Tannenbaum A (2012) A 3d interactive multi-object segmentation tool using local robust statistics driven active contours. Med Image Anal 16(6):1216–1227
9. He L, Peng Z, Everding B, Wang X, Han C, Weiss K, Wee W (2008) A comparative study of deformable contour methods on medical image segmentation. Image Vis Comput 26(2):141–163
10. Kass M, Witkin A, Terzopoulos D (1988) Snakes: active contour models. Int J Comput Vis 1(4):321–331
11. Landman B, Warfield S (2012) Miccai 2012 workshop on multi-atlas labeling. In: Medical image computing and computer assisted intervention conference 2012: MICCAI 2012 grand challenge and workshop on multi-atlas labeling challenge results
12. Liu HT, Sheu TW, Chang HH (2013) Automatic segmentation of brain MR images using an adaptive balloon snake model with fuzzy classification. Med Biol Eng Comput 51(10):1091–1104
13. McInerney T, Terzopoulos D (2000) T-snakes: topology adaptive snakes. Med Image Anal 4(2):73–91
14. Namias R, Bellemare ME, Rahim M, Pirró N (2014a) Uterus segmentation in dynamic MRI using lbp texture descriptors. In: SPIE medical imaging, international society for optics and photonics, pp 90,343W–90,343W
15. Namias R, D'Amato J, del Fresno M, Vénere M (2014b) Automatic rectum limit detection by anatomical markers correlation. Comput Med Imaging Graph 38(4):245–250
16. Okada T, Linguraru MG, Hori M, Suzuki Y, Summers RM, Tomiyama N, Sato Y (2012) Multi-organ segmentation in abdominal ct images. In: 2012 annual international conference of the IEEE engineering in medicine and biology society (EMBC). IEEE, pp 3986–3989
17. Pirro N, Bellemare M, Rahim M, Durieux O, Sielezneff I, Sastre B, Champsaur P (2009) Résultats préliminaires et perspectives de la modélisation dynamique pelvienne patient-spécifique. Pelvi-périnéologie 4(1):15–21
18. Rahim M, Bellemare ME, Bulot R, Pirró N (2010) Pelvic organs dynamic feature analysis for MRI sequence discrimination. In: 2010 20th international conference on pattern recognition (ICPR). IEEE, pp 2496–2499
19. Shang Y, Yang X, Zhu L, Deklerck R, Nyssen E (2008) Region competition based active contour for medical object extraction. Comput Med Imaging Graph 32(2):109–117
20. Soler L, Hostettler A, Agnus V, Charnoz A, Fasquel J, Moreau J, Osswald A, Bouhadjar M, Marescaux J (2012) 3d image reconstruction for comparison of algorithm database: a patient-specific anatomical and medical image database
21. Teschner M, Kimmerle S, Heidelberger B, Zachmann G, Raghupathi L, Fuhrmann A, Cani MP, Faure F, Magnenat-Thalmann N, Strasser W et al (2005) Collision detection for deformable objects. In: Computer graphics forum, vol 24. Wiley Online Library, pp 61–81
22. Vu D, Ha T, Song M, Kim J, Choi S, Chaudhry A (2013) Generalized chan-vese model for image segmentation with multiple regions. Life Sci J 10(1):1889–1895
23. Xu C, Prince JL (1997) Gradient vector flow: A new external force for snakes. In: Proceedings of IEEE computer society conference on computer vision and pattern recognition, 1997. IEEE, pp 66–71
24. Yang H, Zhao L, Tang S, Wang Y (2013) Survey on brain tumor segmentation methods. In: 2013 IEEE international conference on medical imaging physics and engineering (ICMIPE). IEEE, pp 140–145
25. Yoo TS, Ackerman MJ, Lorensen WE, Schroeder W, Chalana V, Aylward S, Metaxas D, Whitaker R (2002) Engineering and algorithm design for an image processing API: a technical report on itk-the insight toolkit. Studies in health technology and informatics pp 586–592

Rafael Namías recieved his Ph.D. in Computer Science from Rosario National University, Rosario, Argentina, in 2015. He is currently doing a posdoc at Centro Internacional Franco Argentino de Ciencias de la Información y Sistemas (CIFASIS). His research interests are in the areas of medical imaging, segmentation, and feature analysis.

Juan Pablo D'Amato recieved his Ph.D. in Computational and Industrial Mathematics in 2011 at the UNICEN University (Tandil, Argentina). He is a Assistant Professor in Computer Graphics courses and has worked in the development of real-time systems and simulators for the Argentine Army Forces. His main research interests include geometry, high performance in GPUs, visualization, and virtual reality applied to training.

Mariana del Fresno received her Ph.D. (2008) at the UNICEN University (Tandil, Argentina). Currently she is Professor in the Department of Computer Science at the same University and member of the Comisión de Investigaciones Científicas de la Provincia de Buenos Aires. Her research interests include medical image processing, segmentation, and visualization.

Marcelo Vénere holds a Ph.D. in Nuclear Engineering from Balseiro Institute, Argentina. He is an Associate Professor in Computer Graphics and Algorithms courses at the UNICEN University (Tandil, Argentina). He is leading several projects in arterial fluid simulation, real-time training, and computer graphics, among other topics. He is the Co-Director of the PLADEMA Research Institute of the UNICEN University at Tandil, Argentina.

Nicola Pirró is a digestive system and general surgeon at Hôpital de la Timone in Marseille, France. He is a Professor in Faculté de Médecine—Aix Marseille Université. His research interests are in the areas of pancreatic diseases and pelvic organ prolapse.

Marc-Emmanuel Bellemare holds a Ph.D. in telecommunication, signal and image processing at Rennes University. He is an Associate Professor in Aix Marseille Université- Polytech' Marseille Dpt GII. His research interests include medical imaging analysis, computer-assisted surgery, and biomedical engineering.